

Improper flexoelectricity in hexagonal rare-earth ferrites

Xin Li^{1†}, Guodong Ren^{2†}, Yu Yun¹, Arashdeep Singh Thind², Amit Kumar Shah¹, Abbey Bowers¹, Rohan Mishra^{3,2*}, Xiaoshan Xu^{1,4*}

¹Department of Physics and Astronomy, University of Nebraska, Lincoln, Nebraska 68588, USA

²Institute of Materials Science & Engineering, Washington University in St. Louis, St. Louis MO, USA

³Department of Mechanical Engineering & Materials Science, Washington University in St. Louis, St. Louis MO, USA

⁴Nebraska Center for Materials and Nanoscience, University of Nebraska, Lincoln, Nebraska 68588, USA

†These authors contribute equally

*Corresponding author: X.X. (xiaoshan.xu@unl.edu), R.M. (rmishra@wustl.edu)

Abstract:

Flexoelectricity is a universal effect that generates electric polarization due to broken inversion symmetry caused by local strain gradient. The large strain gradient at nanoscale makes flexoelectric effects, especially in nanoscopic ferroelectric materials, promising in sensors, actuator, energy harvesting, and memory applications. In this work, we studied flexoelectricity in hexagonal ferrites h-YbFeO₃, an improper ferroelectric expected to have weak piezoelectricity and low sensitivity to depolarization field, which are advantageous for studying intrinsic flexoelectric effects. We show that in h-YbFeO₃ epitaxial thin films, strain gradient is on the order of 10⁶ m⁻¹ occurs near grain boundaries and edge dislocation, which has a significant impact on the non-polar K₃ structural distortion that induces spontaneous polarization. The phenomenological model based on the Landau theory of improper ferroelectricity suggests an indirect flexoelectric effect on the order of 10 nC/m in h-YbFeO₃, which is substantially larger than the expectation from Kogan's mechanism. These results reveal a novel microscopic mechanism of coupling between strain gradient and polarization mediated by structural distortion, which we call improper flexoelectricity.

Flexoelectricity is a fundamental electromechanical effect characterized by the breaking of inversion symmetry due to a strain gradient, leading to the generation of electric polarization.¹⁻⁷ It is universal to any dielectric material, unlike piezoelectricity, which is the coupling between uniform strain and polarization, and is only displayed by non-centrosymmetric crystals. Bulk materials normally have negligibly small strain gradients due to their large strain relaxation length.^{8,9} Therefore, their flexoelectric response is negligible.¹⁰⁻¹⁷ On the nanoscale, however, sizable flexoelectric effects are observed due to the large strain gradients imposed by nonuniform distortions.¹⁸⁻³⁰ In particular, strong flexoelectric effects in ferroelectric materials, which exhibit spontaneous polarization, enable mechanical switching of local polarization.^{24-26,31,32} These promising effects have spurred a number of proposed applications, including as electromechanical sensors, actuators, nanogenerators³⁰, and devices for information storage.^{2,3}

Most studies on flexoelectricity in ferroelectric materials have been focused on perovskite materials showing proper ferroelectricity.^{8,18,19,21-23,31-34} In this context, the flexoelectric coefficients, defined as $\mu = P/\eta$, are often estimated using Kogan's relation in terms of an electric potential difference caused by a strain gradient η and the subsequently induced polarization P .³⁵ This relation can not only estimate the flexoelectric response of bulk ferroelectrics, it can also explain the large μ observed in relaxor ferroelectrics, wherein the nanopolar domains give rise to a large η .³⁶ Experimental measurement of flexoelectric effects and their theoretical prediction are challenging, and the flexoelectric response of dielectrics, beyond the classical proper ferroelectrics having the perovskite structure, are limited^{28,37-41}. Moreover, the microscopic picture of flexoelectric coupling between strain gradient and non-polar order parameter beyond Kogan's mechanism is still absent.

Here, we focus on the flexoelectric response of improper ferroelectrics with the hexagonal rare-earth ferrite (h - R FeO₃, R = Ho-Lu, Y, Sc) structure⁴². The atomic structure of h -RFeO₃ consists of a triangular lattice of FeO₅ bipyramids that are sandwiched between rare earth layers. Below \sim 1000 K, hexagonal ferrites undergo a coupled non-polar K₃ structural distortion and polar Γ_2^- distortion from a centrosymmetric $P6_3/mmc$ structure,⁴³ which features the collective rotation of FeO₅ bipyramids and the buckling of the rare earth layers. The coupling between the K₃ distortion and the polar Γ_2^- mode with imbalanced displacements of rare-earth layer along the c axis leads to a spontaneous polarization ($\approx 10 \mu\text{C}/\text{cm}^2$) and the improper ferroelectric order (see **Fig. 1a**)⁴⁴⁻⁴⁶. Below \sim 150 K, assisted by the K₃ distortion mode, hexagonal ferrites develop a 120-degree antiferromagnetic order with weak ferromagnetism, making them multiferroic.⁴⁷⁻⁴⁹ Due to the improper nature of ferroelectricity, h -RFeO₃ have small piezoelectric coefficients⁵⁰, and are less susceptible to depolarization field, which makes them advantageous to achieve large flexoelectric effects at the nanoscale, unlike proper ferroelectrics where the polarization is quenched at nanoscale dimensions⁴⁴. If a gaint strain gradient can be realized in h -RFeO₃, intrinsic flexoelectricity can be extracted from the variation of the K₃ structural distortion, which consists of large atomic displacements ($\approx 0.5 \text{ \AA}$)^{44,46}, given that the relationship between K₃ distortion and polarization has been well established.

In this work, we demonstrate a novel mechanism of flexoelectricity based on improper ferroelectricity in h -YbFeO₃, which we call improper flexoelectricity. Using atomic resolution scanning transmission electron microscope (STEM) imaging, we show that near both grain boundaries and edge dislocation, the large strain gradient ($\sim 10^6 \text{ m}^{-1}$) strongly suppresses the magnitude of the

K_3 distortion, which is consistent with the phenomenological Landau theory-based model of improper ferroelectricity. The observed correlation between strain gradient and phases of the K_3 distortion or polarization directions originates from the stable and metastable state on energy landscape, suggesting a bias imposed by the strain gradient which breaks the inversion symmetry. The flexoelectric coefficient (~ 10 nC/m) that is 1-2 orders of magnitude larger than that estimated from the Kogan's mechanism for h-YbFeO₃.

The K_3 structural distortion in h-RFeO₃ can be described with a magnitude Q , and the direction of in-plane displacement of the apical oxygen atoms using an angle (or phase) ϕ , as shown in **Fig. 1b**. The free energy of the hexagonal ferrites with the double order parameters, Q and ϕ , can be written as:⁵¹

$$F = \frac{a}{2}Q^2 + \frac{b}{4}Q^4 - gQ^3P \cos(3\phi) + \frac{g_P}{2}Q^2P^2 + \frac{a_P}{2}P^2, \quad (1)$$

where Q and ϕ are the magnitude and the phase of the K_3 distortion, P is the magnitude of the polar distortion (Γ_2^-) that is proportional to polarization P , and a , b , g , and g' are coefficients. As the first two terms dominate, minimization of the free energy with respect to Q leads to $Q_{min} \approx Q_0 = \sqrt{\frac{-a}{b}}$, where $a < 0$, $b > 0$. The next two terms in Eq. (1) describe the coupling between the Γ_2^- and the K_3 structural distortions. Minimization of the free energy with respect to P leads to:

$$P_{min} = \frac{gQ_{min}^3 \cos(3\phi)}{a_P + g_P Q_{min}^2}, \quad (2)$$

The calculated energy landscape (using the parameters in Ref.⁵⁰) has six energy minima, corresponding to $\phi = 2n\pi/3$ (n is integer) for $P_{min} = P_0$ and $\phi = (2n+1)\pi/3$ for $P_{min} = -P_0$, as shown in **Fig. 1c**, where $P_0 = \frac{gQ_0^3}{a_P + g_P Q_0^2}$.

Depending on the nature of the strain gradient, it can break different inversion symmetries and change the magnitude Q of the K_3 structural distortion in h-YbFeO₃. Given the strong coupling of K_3 mode with the polar Γ_2^- mode, we look into the effect of a strain gradient on the energy landscape described by the Landau model. The corresponding free energy can be written as (see details in Supplementary Materials Section 2):

$$F_{flexo} = \frac{f_1}{2}Q^2\eta^2 + f_2Q^3 \cos(3\phi)\eta, \quad (3)$$

where η is a general symbol for strain gradient, f_1 and f_2 are coupling coefficients. The addition of the term $\frac{f_1}{2}Q^2\eta^2$ to Eq. (1) changes the K_3 distortion magnitude to:

$$Q_{min} = \sqrt{\frac{-a - f_1\eta^2}{b}}, \quad (4)$$

for the minimum free energy. The calculated energy landscape in **Fig. 1d** shows that, with $f_1 > 0$, the energy minima occur at $Q_{min} < Q_0$. The term $f_2Q^3 \cos(3\phi)\eta$ in Eq. (3) breaks the symmetry

between $P_{\min} > 0$ and $P_{\min} < 0$ in the energy landscape. With $f_1 = 0$ and $f_2 > 0$, by combining Eq. (1) and Eq. (3), one finds

$$Q_{\min} = \frac{-3f_2\eta \cos(3\phi) + \sqrt{[3f_2\eta \cos(3\phi)]^2 - 4ab}}{2b}. \quad (5)$$

In other words, for strain gradient η , Q_{\min} also depends on the phase ϕ . The calculated energy landscape in **Fig. 1e** shows that, with $f_2\eta < 0$, the three energy minima $\phi = (2n+1)\pi/3$ ($P_{\min} < 0$) become local minimum with $Q_{\min} < Q_0$ while the other three energy minima $\phi = 2n\pi/3$ ($P_{\min} > 0$) remain global with $Q_{\min} > Q_0$. This creates a bias of positive P_{\min} over negative P_{\min} , as if the strain gradient ($\eta > 0$) was an electric field. Similarly with $f_2\eta > 0$, negative P_{\min} is favored.

Assuming $f_1 = 3.7 \times 10^7$ eV/f.u. and $f_2 = -1 \times 10^3$ eV/Å² f.u.) based on the atomic-resolution measurements as shown below and Landau parameters in Ref⁵¹, the dependence of Q_{\min} on η is calculated and plotted in **Fig. 1f**. The strain gradient η splits the Q_{\min} values into a higher stable branch (in solid line) and a lower metastable branch (in dash line). Q_{\min} becomes zero at $\eta_0 = \sqrt{-\frac{a}{f_1}}$, corresponding to total quenching of the K_3 distortion. **Fig. 1g** is the calculated η dependence of P_{\min} . Again, the presence of positive η reduces the negative P_{\min} branch more effectively than it does on the positive P_{\min} branch. For $\eta f_2 < 0$, the positive P_{\min} branch is favored. Therefore, in improper ferroelectric hexagonal ferrites or isomorphic manganites, it is expected that by coupling to structural distortions, strain gradient η can reduce the structural distortion and favor a certain direction of polarization, which leads to an improper flexoelectric effect.

Large strain gradients can only exist in regions where the crystal undergoes dramatic spatial changes such as near dislocations and grain boundaries^{19,21,22,52}. As illustrated in **Fig. 2a**, near a grain boundary, the basal plane of the h-RFeO₃ unit cells is bent. The deviation of the *c* axis (polar axis) from the vertical direction can be described by a small bending angle θ , which is approximately equal to the shear strain e_{zx} . θ is larger near the grain boundary and smaller away from the boundary, suggesting a strain gradient $\eta = \frac{\partial e_{zx}}{\partial x}$. The schematic atomic structure for the bent half-layer is given in **Fig. 2b**. **Fig. 2c** shows a high-angle annular dark-field scanning transmission electron microscope (HAADF-STEM) image of the atomic structure of h-YbFeO₃ near a grain boundary viewed along the [100] direction. The existence of YbFe₂O₄ stacking faults, which are highlighted by dashed rectangular boxes, as well as the long-range bending of h-YbFeO₃ can be identified near the grain boundary due to vertical mismatch. Close-up views of a strongly and a weakly bent region are given in I and II, respectively. The comparison between area I and area II confirms the variation of θ : larger θ near the grain boundary and smaller θ far away from the boundary. It should be noticed that though the multidomain or topological strip domain states are formed under the influence of shear strain^[51,53] (see spatial mapping of ϕ in **Fig. S10 b**), the polarization is favored to up direction in strong bending region near grain boundary.

Using the FeO layer, which is flat in the unstrained structure (unlike the buckled Yb layer), we calculated the θ values as a function of position (see Supplementary Materials Section 3). It turns out that θ depends primarily on the position x (along [-211] direction). In particular, the difference in θ in the regions I and II is 4 ± 0.5 deg (see **Fig. 3 a**). Furthermore, we calculated local

strain gradient $\eta = \frac{\partial e_{zx}}{\partial x} = \frac{\partial \theta}{\partial x}$. The results are shown in **Fig. 3b** as a 2D map, where the maximum value of η reaches $6 \times 10^6 \text{ m}^{-1}$.

The corrugation of the rare earth layers (Q') is a representative component of the K_3 distortion ($Q' \approx 0.4 Q$)^{54,55}. In **Fig. 3c**, Q' values are calculated and overlaid on the image for the area with bent lattice. Clearly, Q' values are smaller in the bent lattice compared to the regions that don't have a noticeable strain gradient (see **Fig. S10 a**). More specifically, from right to left, as the strain gradient increases (see **Fig. 3b**), Q' decreases from $\approx 35 \text{ pm}$ to less than 10 pm , suggesting that the strong strain gradient is correlated with the suppression of Q' . **Fig. 3d** displays the Q' and ϕ values of flat lattice in a polar plot. Here ϕ values are concentrated around 120° , indicating a single domain of positive polarization (see **Fig. 1c**). The Q' values have a narrow distribution around 40 pm . On the contrary, in the polar plot **Fig. 3e** for the bent region, a clear distribution of both Q' and ϕ is visible. In addition to bending regions near grain boundaries, the similar magnitude of bending angle and strain gradients also exist near edge dislocation (see Supplementary Materials Section 3, 4), associated suppression of Q' indicates the effect of improper flexoelectricity is independent of the type of defects which induces the bending.

The quantitative correlation between Q' and η is plotted in **Fig. 4a**; the bent areas come from two different regions near the grain boundary and edge dislocation (see **Fig. S2** and **Fig. S6**). The suppression of Q' in the severely bent region indicates a significant effect of the f_1 term in F_{flexo} . By fitting the observation in **Fig. 4a** using Eq. (4) and $Q' \approx 0.4Q_{\text{min}}$, one finds $f_1 = (3.7 \pm 0.5) \times 10^7 \text{ eV/f.u}$. The quantitative correlation between P and η can be calculated using Eq. (2). The results are plotted in **Fig. 4b**. Overall, P decreases with $|\eta|$, which is due to the reduction of Q' . Electric polarization can be roughly estimated using $P = P_0 \frac{P}{P_0}$. Here we assume $P_0 = 10 \mu\text{C/cm}^2$ found experimentally for the unstrained lattice of h-YbFeO₃^{42,53}, $P_0 = 0.16 \text{ \AA}$ according to first-principles calculations⁵⁶. With the polarization estimated, one can calculate average flexoelectric coefficient $\bar{\mu} = \frac{\Delta P}{\Delta \eta}$. According to **Fig. 4b**, polarization is reduced to zero with a strain gradient $\eta_0 = 2.5 \pm 0.5 \times 10^6 \text{ m}^{-1}$. Hence, one finds average $\bar{\mu} \approx \frac{P_0}{\eta_0} = 40 \pm 10 \text{ nC/m}$.

Notice that the flexoelectric effect reported here is an indirect effect due to the coupling between strain gradient η and the magnitude Q of the non-polar K_3 structural distortion, described with the f_1 term in Eq. (3). The clear η dependence allows for the determination of f_1 . The effect of the f_2 term is, however, mainly to split Q and P into a stable branch and a metastable branch. As shown in **Fig. 4b**, when the magnitude of strain gradient is larger than $\sim 2 \times 10^6 \text{ m}^{-1}$, the large positive (negative) strain gradient tends to favor the positive (negative) P , which is consistent with the theoretical expectation for the biasing effect of strain gradient which breaks the inversion symmetry. Moreover, under lower strain gradient, the distribution of polarization states on metastable branch can be interpreted as the convolution of improper flexoelectricity and shear strain-induced topological stripe domain state^{51,53}, where the suppression of P still follows the model.

One can estimate the flexoelectric coefficient using Kogan's method,³⁵ which says $\mu = f' \chi$, where χ is the electric susceptibility and f' is the electric potential generated per unit strain gradient. Kogan derived that $f' = 1-10 \text{ V}$ for most materials.³⁵ Taking $\chi \approx 30 \varepsilon_0$ for h-YbFeO₃⁴⁴, where ε_0 is

the vacuum permittivity, one finds that $\mu = 0.3\text{-}3 \text{ nC/m}$. This result is one or two orders of magnitude smaller than the $\bar{\mu}$ value estimated above using experimentally observed atomic displacements, confirming that the improper flexoelectricity is distinct from the generic Kogan mechanism.

In summary, the nanoscopic large strain gradient was observed in h-YbFeO₃ films near the grain boundaries and edge dislocation, and the correlation between the strain gradient and the primary order parameters suggests a giant flexoelectric effect in h-YbFeO₃. Based on a phenomenological model, at least two coupling mechanisms are identified, in which strain gradient suppresses non-polar K₃ structural distortion and biases the secondary polarization, respectively. The improper flexoelectricity, corresponding to the indirect electromechanical coupling between polarization and strain gradient, offers new insight into the microscopic origin of flexoelectric effects in improper ferroelectric hexagonal ferrites or manganites beyond conventional Kogan's mechanism.

Acknowledgements

Funding: This work was primarily supported by the National Science Foundation (NSF), Division of Materials Research (DMR) under Grant Nos. DMR-1454618 and DMR-2145797, and by the Nebraska Center for Energy Sciences Research. The research was performed in part in the Nebraska Nanoscale Facility: National Nanotechnology Coordinated Infrastructure and the Nebraska Center for Materials and Nanoscience, which are supported by the NSF under Grant No. ECCS- 2025298, and the Nebraska Research Initiative. The Microscopy work was conducted as part of a user project at the Center for Nanophase Materials Sciences (CNMS), which is a US Department of Energy, Office of Science User Facility at Oak Ridge National Laboratory.

Author contributions

The thin film synthesis and x-ray diffractions were carried out by X.L. and Y.Y. under the supervision of X.X. (S)TEM experiments were conducted by G.R. and A.S.T. under the supervision of R.M. The study was conceived by X.L. and X.X. X.L., G.R., Y.Y, R.M, and X.X. co-wrote the manuscript. All the authors discussed the results and commented on the manuscript.

Competing interests

The authors declare no competing interest.

Reference:

1. Wang, B., Gu, Y., Zhang, S. & Chen, L.-Q. Flexoelectricity in solids: Progress, challenges, and perspectives. *Prog Mater Sci* 106, 100570 (2019).

2. Tripathy, A., Saravanakumar, B., Mohanty, S., Nayak, S. K. & Ramadoss, A. Comprehensive Review on Flexoelectric Energy Harvesting Technology: Mechanisms, Device Configurations, and Potential Applications. *ACS Appl Electron Mater* 3, 2898–2924 (2021).
3. Shu, L. et al. Flexoelectric materials and their related applications: A focused review. *Journal of Advanced Ceramics* 8, 153–173 (2019).
4. Lee, D. Flexoelectricity in thin films and membranes of complex oxides. *APL Mater* 8, (2020).
5. Nguyen, T. D., Mao, S., Yeh, Y., Purohit, P. K. & McAlpine, M. C. Nanoscale Flexoelectricity. *Advanced Materials* 25, 946–974 (2013).
6. A. K. Tagantsev. Piezoelectricity and flexoelectricity in crystalline dielectrics. *Phys. Rev. B* 36, 6177 (1987).
7. Zubko, P., Catalan, G. & Tagantsev, A. K. Flexoelectric Effect in Solids. *Annu Rev Mater Res* 43, 387–421 (2013).
8. Bhaskar, U. K. et al. A flexoelectric microelectromechanical system on silicon. *Nat Nanotechnol* 11, 263–266 (2016).
9. Zubko, P., Catalan, G., Buckley, A., Welche, P. R. L. & Scott, J. F. Strain-Gradient-Induced Polarization in SrTiO₃ Single Crystals. *Phys Rev Lett* 99, 167601 (2007).
10. Gruverman, A., Wu, D. & Scott, J. F. Piezoresponse force microscopy studies of switching behavior of ferroelectric capacitors on a 100-ns time scale. *Phys Rev Lett* 100, 097601 (2008).
11. Rodriguez, B. J., Gruverman, A., Kingon, A. I., Nemanich, R. J. & Cross, J. S. Investigation of the mechanism of polarization switching in ferroelectric capacitors by three-dimensional piezoresponse force microscopy. *Applied Physics A* 80, 99–103 (2005).
12. Gruverman, A. & Kalinin, S. V. Piezoresponse force microscopy and recent advances in nanoscale studies of ferroelectrics. *J Mater Sci* 41, 107–116 (2006).
13. Bonnell, D. A., Kalinin, S. V., Khoklin, A. L. & Gruverman, A. Piezoresponse Force Microscopy: A Window into Electromechanical Behavior at the Nanoscale. *MRS Bull* 34, 648–657 (2009).
14. Fujisawa, H., Yagi, T., Shimizu, M. & Niu, H. Investigation of polarization switching processes in Pb(Zr,Ti)O₃ capacitors using piezoresponse imaging. *Ferroelectrics* 269, 21–26 (2002).

15. Fujisawa, H., Shimizu, M. & Niu, H. Piezoresponse force microscopy observations of switching behavior in $\text{Pb}(\text{Zr},\text{Ti})\text{O}_3$ capacitors. *Jpn J Appl Phys* 43, 6571–6575 (2004).
16. Jungk, T., Hoffmann, Á. & Soergel, E. Quantitative analysis of ferroelectric domain imaging with piezoresponse force microscopy. *Appl Phys Lett* 89, 89–91 (2006).
17. Jesse, S., Baddorf, A. P. & Kalinin, S. V. Switching spectroscopy piezoresponse force microscopy of ferroelectric materials. *Appl Phys Lett* 88, 062908 (2006).
18. Liu, Y. et al. Giant room temperature compression and bending in ferroelectric oxide pillars. *Nat Commun* 13, 335 (2022).
19. Catalan, G. et al. Flexoelectric rotation of polarization in ferroelectric thin films. *Nat Mater* 10, 963–967 (2011).
20. Lee, D. et al. Giant Flexoelectric Effect in Ferroelectric Epitaxial Thin Films. *Phys Rev Lett* 107, 057602 (2011).
21. Gao, P. et al. Atomic-Scale Measurement of Flexoelectric Polarization at SrTiO_3 Dislocations. *Phys Rev Lett* 120, 267601 (2018).
22. Wu, M. et al. Engineering of atomic-scale flexoelectricity at grain boundaries. *Nat Commun* 13, 216 (2022).
23. Cai, S. et al. Enhanced polarization and abnormal flexural deformation in bent freestanding perovskite oxides. *Nat Commun* 13, 5116 (2022).
24. Ming, W. et al. Flexoelectric engineering of van der Waals ferroelectric CuInP_2S_6 . *Sci Adv* 8, 1232 (2022).
25. Lee, J. H. et al. Flexoelectricity-Driven Mechanical Switching of Polarization in Metastable Ferroelectrics. *Phys Rev Lett* 129, 117601 (2022).
26. Guan, Z. et al. Mechanical Polarization Switching in $\text{Hf}_{0.5}\text{Zr}_{0.5}\text{O}_2$ Thin Film. *Nano Lett* 22, 4792–4799 (2022).
27. C. A. Mizzi, A. Y. W. Lin, and L. D. Marks. Does Flexoelectricity Drive Triboelectricity? *Phys. Rev. Lett.* 123, 116103 (2019).
28. P. Koirala, C. A. Mizzi, L. D. Marks. Direct Observation of Large Flexoelectric Bending at the Nanoscale in Lanthanide Scandates. *Nano Lett.* 18, 3850–3856 (2018).
29. Matteo Springolo, Miquel Royo, and Massimiliano Stengel. Direct and Converse Flexoelectricity in Two-Dimensional Materials. *Phys. Rev. Lett.* 127, 216801 (2021).

30. Chinmayee Chowde Gowda, John Cavin, Partha Kumbhakar, Chandra Sekhar Tiwary, Rohan Mishra. Flexible Nanogenerators Based on Enhanced Flexoelectricity in Mn₃O₄ Membranes. *Small* 20, 2307167(2024).

31. Park, S. M. et al. Selective control of multiple ferroelectric switching pathways using a trailing flexoelectric field. *Nat Nanotechnol* 13, 366–370 (2018).

32. Lu, H. et al. Mechanical writing of ferroelectric polarization. *Science* (1979) 335, 59–61 (2012).

33. Li, Q. et al. Quantification of flexoelectricity in PbTiO₃/SrTiO₃ superlattice polar vortices using machine learning and phase-field modeling. *Nat Commun* 8, 1468 (2017).

34. Morozovska, A. N., Eliseev, E. A., Kalinin, S. V. & Hertel, R. Flexosensitive polarization vortices in thin ferroelectric films. *Phys Rev B* 104, 085420 (2021).

35. Kogan S.M. Piezoelectric effect during inhomogeneous deformation and acoustic scattering of carriers in crystals. *Sov. Phys. Solid State* 5, 2069–2070 (1964).

36. Ma, W. & Cross, L. E. Observation of the flexoelectric effect in relaxor Pb(Mg_{1/3}Nb_{2/3})O₃ ceramics. *Appl Phys Lett* 78, 2920–2921 (2001).

37. P. Jiao, H.Cheng, J. Li. et al Flexoelectricity-stabilized ferroelectric phase with enhanced reliability in ultrathin La:HfO₂ films. *Appl. Phys. Rev.* 10, 031417 (2023).

38. C. J. Brennan, O.R. Ghosh, K. Koul. Out-of-Plane Electromechanical Response of Monolayer Molybdenum Disulfide Measured by Piezoresponse Force Microscopy. *Nano Lett.* 17, 5464–5471 (2017).

39. Narvaez, J., Vasquez-Sancho, F. & Catalan, G. Enhanced flexoelectric-like response in oxide semiconductors. *Nature* 538, 219–221 (2016).

40. Kanghyun Chu and Chan-Ho Yang. Nonlinear flexoelectricity in noncentrosymmetric crystals. *Phys. Rev. B* 96, 104102 (2017).

41. Ya-Xun Wang, Jian-Gao Li, Gotthard Seifert, Kai Chang, Dong-Bo Zhang. Giant Flexoelectricity in Bent Semiconductor Thinfilm. *Nano Lett.* 24, 411–416 (2024).

42. Xin Li, Yu Yun, Xiaoshan Xu. Recent Progress on Multiferroic Hexagonal Rare-Earth Ferrites (h-RFeO₃, R= Y, Dy-Lu). *J. Phys. D: Appl. Phys.* 58 073003 (2025).

43. Wang, W. et al. Room-Temperature Multiferroic Hexagonal LuFeO₃ Films. *Phys Rev Lett* 110, 237601 (2013).

44. Yun, Y. et al. Spontaneous Polarization in an Ultrathin Improper-Ferroelectric/Dielectric Bilayer in a Capacitor Structure at Cryogenic Temperatures. *Phys Rev Appl* 18, 34071 (2022).

45. Li, X., Yun, Y. & Xu, X. Improper ferroelectricity in ultrathin hexagonal ferrites films. *Appl Phys Lett* 122, 182901 (2023).

46. Fennie, C. J. & Rabe, K. M. Ferroelectric transition in YMnO₃ from first principles. *Phys Rev B* 72, 100103 (2005).

47. Sinha, K. et al. Tuning the Neel Temperature of Hexagonal Ferrites by Structural Distortion. *Phys Rev Lett* 121, 237203 (2018).

48. Li, X., Yun, Y., Thind, A.S. et al. Domain-wall magnetoelectric coupling in multiferroic hexagonal YbFeO₃ films. *Sci Rep* 13, 1755 (2023).

49. Disseler, S. M. et al. Magnetic Structure and Ordering of Multiferroic Hexagonal LuFeO₃. *Phys Rev Lett* 114, 217602 (2015).

50. Martin Lilienblum. Ferroelectric order in multiferroic hexagonal manganites. Universität Bonn (2016).

51. Artyukhin, S., Delaney, K. T., Spaldin, N. A. & Mostovoy, M. Landau theory of topological defects in multiferroic hexagonal manganites. *Nat Mater* 13, 42–49 (2014).

52. Ren, G., Omprakash, P., Li, X., et al. Polarization Pinning at an Antiphase Boundary in Multiferroic YbFeO₃. *Chinese Phys. B* 33 118502 (2024)

53. X. Wang, M. Mostovoy, M. G. Han, Y. Horibe1, T. Aoki, Y. Zhu, and S.-W. Cheong. Unfolding of Vortices into Topological Stripes in a Multiferroic Material. *Phys. Rev. Lett.* 112, 247601 (2014)

54. Megan E Holtz. et al. Topological Defects in Hexagonal Manganites: Inner Structure and Emergent Electrostatics. *Nano Lett* 17, 5883–5890 (2017).

55. Megan E Holtz, Elliot S Padgett, Rachel Steinhardt, Charles M Brooks, Dennis Meier, Darrell G Schlom, David A Muller, Julia A Mundy. Dimensionality-induced change in topological order in multiferroic oxide superlattices. *Phys. Rev. Lett.* 126, 157601(2021).

56. Das, H., Wysocki, A. L., Geng, Y., Wu, W. & Fennie, C. J. Bulk magnetoelectricity in the hexagonal manganites and ferrites. *Nat Commun* 5, 2998 (2014).

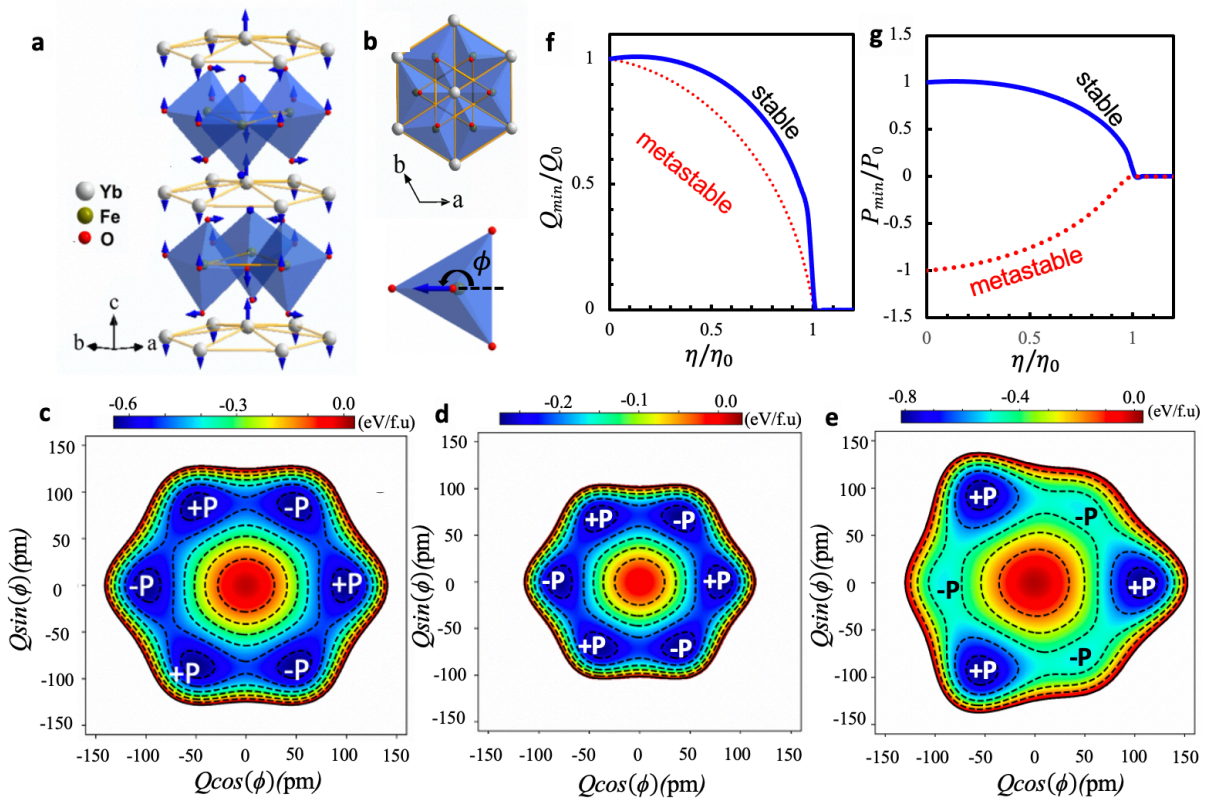


Fig. 1 Phenomenological model of flexoelectricity in h-RFeO₃. (a) Atomic structure of the improper ferroelectric h-YbFeO₃. The arrows indicate the displacement of atoms. (b) In-plane view of h-RFeO₃ and the displacement of apical oxygen within FeO₅ bipyramidal, corresponding to order parameters (Q, ϕ). The energy landscape with $f_1 = f_2 = 0$ in (c), $f_1 = 3.7 \times 10^7$ eV/f.u., $f_2 = 0$, and $\eta = 1 \times 10^6$ m⁻¹ in (d), and $f_1 = 0, f_2 = -1 \times 10^3$ eV/Å² f.u., and $\eta = 1 \times 10^6$ m⁻¹ in (e) respectively. (f) and (g) are the dependence of Q_{\min} and P_{\min} (see text) on the strain gradient η , assuming $f_1 = 3.7 \times 10^7$ eV/f.u. and $f_2 = -1 \times 10^3$ eV/Å² f.u..

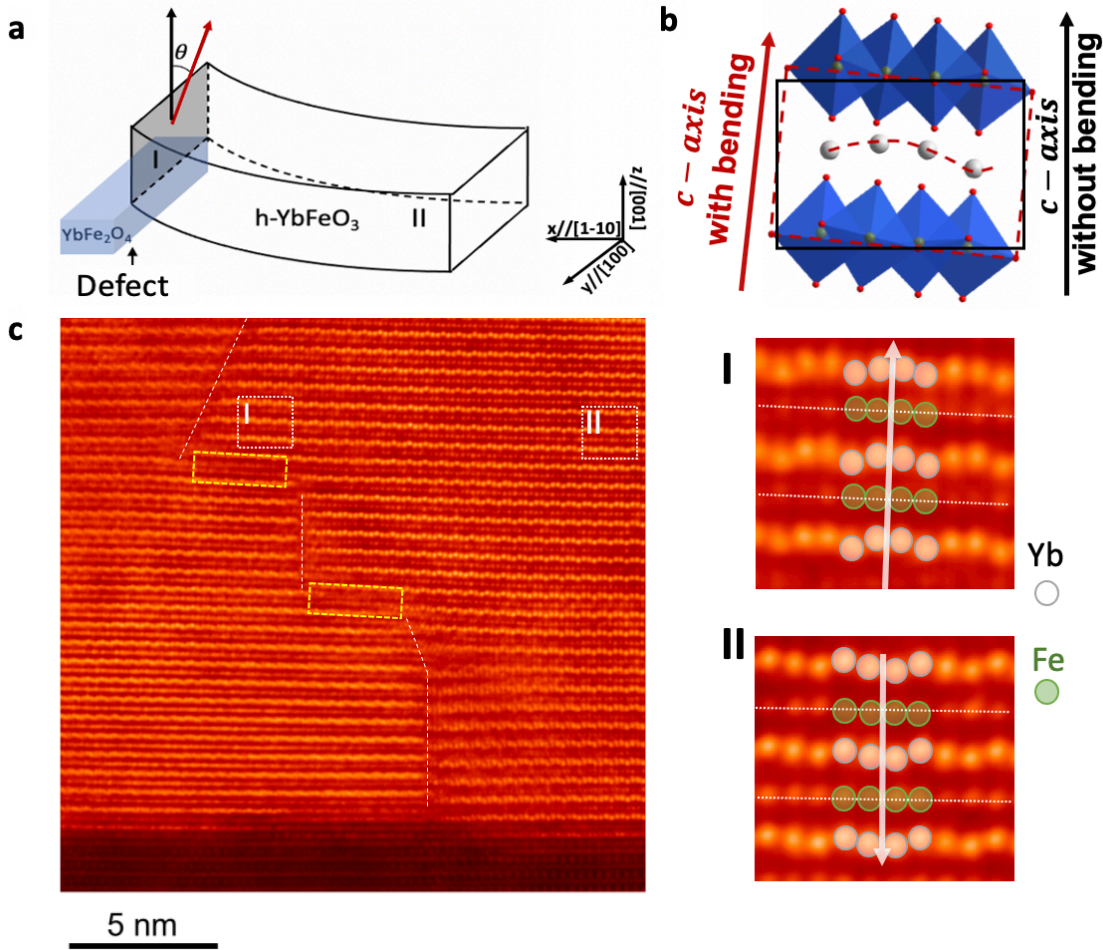


Fig. 2 (a) Schematic of large bending of h-YbFeO₃ due to a h-YbFe₂O₄ grain. θ is the bending angle. (b) The schematic atomic structure of half-layer of h-YbFeO₃ without and with bending. (c) HAADF-STEM image of h-YbFeO₃ thin films showing an area around a grain boundary with YbFe₂O₄ defects. The white dashed line corresponds to the grain boundary and yellow dashed rectangular boxes highlight YbFe₂O₄ defects. Area I and II are close-up views of the areas in (c) indicated by the white dashed boxes. The arrows indicate the polarization direction.

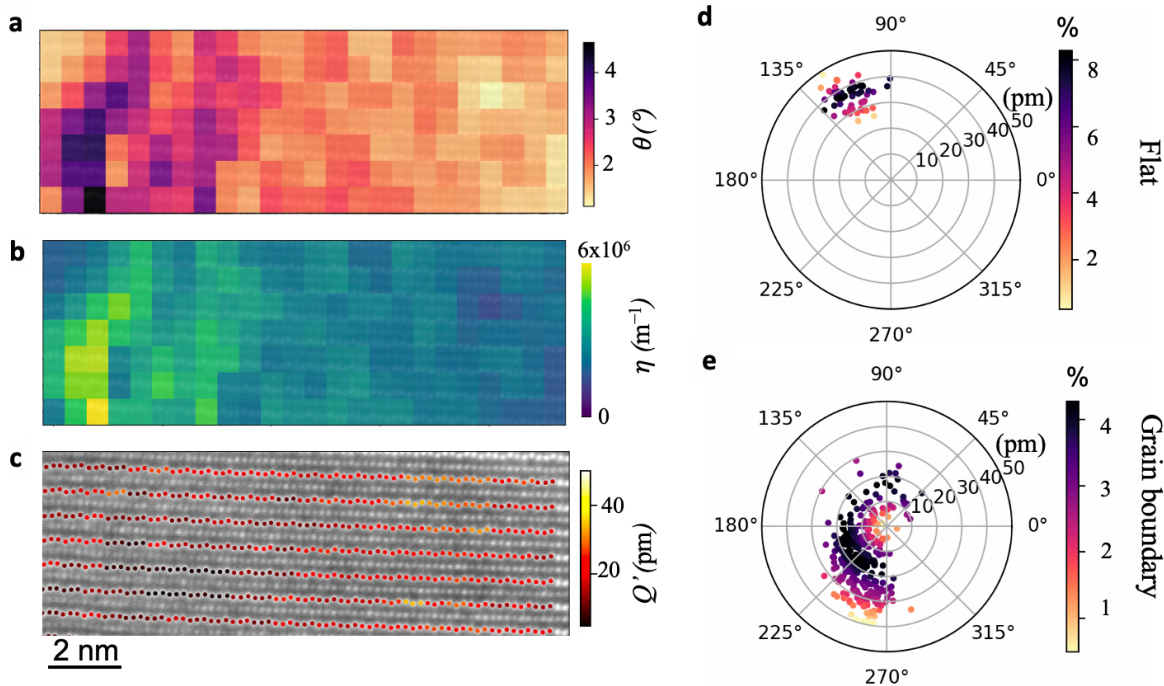


Fig. 3 (a) Spatial mapping of bending angle, (b) strain gradient, and (c) order parameter Q' in the bending region near a grain boundary in h-YbFeO₃. (d) and (e) are pole figures of (Q', Φ) for the flat region and bending region of (c), respectively.

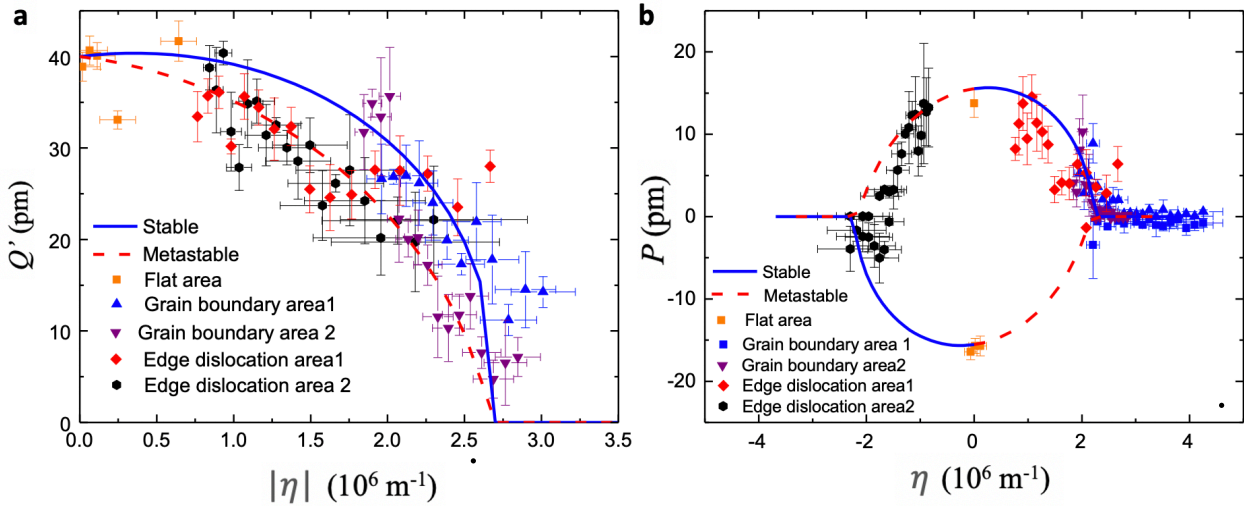


Fig. 4 The dependence of Q' (a) and P (b) on the strain gradient and the fitting with the improper flexoelectricity model.

